LA-UR-20-29896 (Accepted Manuscript)

Characteristics of thermospheric infrasound predicted using ray tracing and weakly non-linear waveform analyses

Blom, Philip Stephen
Waxler, Roger

To be published in: The Journal of the Acoustical Society of America

DOI to publisher's version: 10.1121/10.0004949

Permalink to record: http://permalink.lanl.gov/object/view?what=info:lanl-repo/lareport/LA-UR-20-29896

Characteristics of thermospheric infrasound predicted using ray tracing and weakly non-linear waveform analyses

Philip Blom[1] and Roger Waxler[2]

[1]Los Alamos National Laboratory, Los Alamos, NM 87545 USA

[2]University of Mississippi, University, MS 38655 USA

Last Edited April 9, 2021

Release Number: LA-UR-20-29896

Abstract

Infrasonic signals refracted by thermal gradients in the rarefied upper atmosphere are modeled using a combination of ray tracing and weak shock theory to develop an understanding of thermospheric infrasound signals produced by energetic, transient sources. Canonical arrival structures in the form of u-wave signatures are identified for returns refracted at lower altitudes within the thermosphere and possible multi-pathing produced by effective sound speed inflections are investigated to elucidate more complex arrival structures that are found to be spatially localized. Variability in the source characteristics is investigated and it is found that, while some waveform phase information is lost due to finite amplitude effects, arrival characteristics are strongly dependent on the peak overpressure near the source. Variability in the propagation path is considered using archived atmospheric specifications and implies that despite uncertainties related to the dynamic and sparsely sampled nature of the atmosphere, thermospheric signatures might be useful in estimating the yield for explosive sources. Lastly, thermospheric arrivals from a failed rocket launch as well as those from several large chemical explosions are analyzed and it is found that qualitative trends match those predicted and analyses here provide additional insight into such signatures.

PACS numbers: 43.20.Dm, 43.25.-x

I. Introduction

Infrasonic signals are sound waves at frequencies below the threshold of human hearing that are known to propagate long distances in atmospheric waveguides created by wind and temperature gradients. Infrasonic signals generated at the ground surface or in the low atmosphere are typically refracted upward due to the decreasing temperature through the troposphere. Wind structures at the tropopause and stratopause, termed the jet stream and circumpolar vortex, respectively, can produce downward refraction sufficient to return sound to the ground surface for propagation downwind; however, in many cases signals propagate into the upper atmosphere and return to the ground due to the thermal gradients in the thermosphere (Waxler, 2016; Waxler & Assink, 2019). The rarefied atmosphere in the meso- and thermospheric layers of the atmosphere produce finite amplitude propagation effects that complicate modeling and prediction of infrasonic signals refracted from such altitudes (Rogers & Gardner, 1980; Lonzaga et al., 2015; Scott et al., 2017).

In contrast with signal returns from the troposphere and stratosphere, which are typically characterized by highly dispersed and complex waveforms, thermospheric returns tend to have considerably less structure and are often relatively clean, long period u-waves (Fee et al., 2013; Lalande & Waxler, 2016; Green et al., 2018). The long periods of thermospheric returns can be attributed to finite amplitude (*i.e.* non-linear) propagation effects in which positive phases

propagate faster than negative phases, causing impulses to stretch as they propagate (Rogers & Gardner, 1980; Lonzaga et al., 2015; Scott et al., 2017). The lack of fine structure in thermospheric returns can be attributed to the severe attenuation at higher frequencies found in rarefied gases (Sutherland & Bass, 2004).

In this paper, an overview of the modeling of thermospheric infrasound in the weak shock theory approximation is presented. In weak shock theory, ray tracing is used to predict path geometry and travel time. A second order, non-linear transport equation, which generally reduces to a form of Burger's equation, is used to capture the non-linear propagation effects on the evolution of the waveform structure of the infrasonic arrival, for a given source signal model (Rogers & Gardner, 1980; Lonzaga et al., 2015; Scott et al., 2017). The potential existence of canonical waveform structures, such as those observed in stratospheric returns under pristine conditions (Kulichkov et al., 2004; Evers & Haak, 2007; Waxler et al., 2015), is investigated. Spatial variability of thermospheric propagation paths is also investigated considering the impacts of atmospheric winds in general as well as the presence of lower altitude waveguides. Further, sensitivity of the predicted arrival waveform to the near-source signal is investigated and the dynamic nature of the atmospheric state is considered in a first step to quantify the propagation variability. Lastly, observed infrasonic signals from a series of surface explosions in the southwestern US will be presented and discussed showing how thermospheric propagation modeling can enhance understanding of such signals.

II. Modeling thermospheric infrasound signals

Infrasonic signals propagating large distances through the atmosphere can be modeled using a number of available software tools including ray tracing, parabolic equation, modal expansion, and others (for a recent review see Waxler & Assink, 2019). Acoustics is often understood to be restricted to the study of the linear approximation to fluid mechanics, and propagation models based on the linear approximation are often sufficient. In the case of thermospheric infrasonic signals, however, the rarefied atmosphere in the meso- and thermospheric regions leads to finite amplitude propagation effects, requiring models that go beyond the linear approximation. Existing non-linear propagation models capable of modeling propagation infrasound propagation at thermospheric ranges and altitudes take two forms. There are non-linear extensions of the geometrical acoustics approximation (Rogers & Gardner, 1980; Lonzaga et al., 2015; Scott et al., 2017) and full wave simulations (Sabatini et al., 2016; de Groot-Hedlin, 2008). In this work the geometrical acoustics approach will be used. In this method, ray paths are found in the linear approximation, and then waveform characteristics are estimated by solving a non-linear generalization of the classic transport equation along the ray path.

For the analysis discussed here, the ray tracing methods developed by Blom & Waxler will be applied assuming an atmosphere layer surrounding a spherical globe to more accurately capture the propagation geometry for the increased turning heights of thermospheric propagation paths (Blom & Waxler, 2017; Blom, 2019). The equations governing ray paths are summarized as,

$$\frac{\partial \alpha_j}{\partial s} = \mathcal{G}_j \frac{c_{g,j}}{c_g}, \qquad c_{g,j} = c\frac{\psi_j}{\psi} + v_j, \tag{1a}$$

$$\frac{\partial \psi_j}{\partial s} = -\frac{\mathcal{G}_j}{c_g}\left(\psi \frac{\partial c}{\partial \alpha_j} + \sum_k \psi_k \frac{\partial v_k}{\partial \alpha_j} + \mathcal{T}_j\right), \tag{1b}$$

where $\vec{\alpha}$ denote the curvilinear coordinates, s is the physical ray length, c is the adiabatic sound speed, $\vec{v}$ is the ambient atmospheric wind, $\vec{c}_g$ is the acoustic group velocity along the ray path, ψ_j is the j^{th} component of the eikonal vector (e.g., $r, \theta,$ or ϕ for spherical coordinates), and $\mathcal{G}_j$ and $\mathcal{T}_j$ account for the curvilinear coordinate transformation (Blom, 2019).

In addition to the path geometry, travel time, and losses computed in standard ray tracing analysis, weakly non-linear waveform evolution can be modeled using the Burger's equation along individual ray paths (Rogers & Gardner, 1980; Lonzaga et al., 2015; Scott et al., 2017). The scaled overpressure waveform, $u(s, \tau)$, can be computed using,

$$\frac{\partial u}{\partial s} = \tilde{\beta} u \frac{\partial u}{\partial \tau}, \tag{2a}$$

$$\tilde{\beta}(s) = \beta \frac{p_{\text{ref}}}{\rho_0 c_0^2} \frac{\psi_0 c_0}{c_{g0} c_{\text{src}}} \sqrt{\frac{D_0 \rho_0 c_{g0}^3}{D \rho c_g^3} \frac{c\psi^3}{c_0 \psi_0^3}}, \tag{2b}$$

where s is again ray length, $c_g = |\vec{c}_g|$ is the group velocity magnitude, τ is retarded time of the waveform, $\tilde{\beta}(s)$ is the scaled non-linearity parameter along the ray path, β is the familiar non-linearity parameter, p_{ref} is a defined reference overpressure, ρ is ambient atmospheric density, and D is the Jacobian determinant between ray coordinates (s and launch angles, ϑ and φ) and the original Cartesian coordinates. In this definition, subscript zeros denote values at a reference

location along the ray path at which the waveform is known and c_{src} denotes the sound speed at the actual source location. The introduction of auxiliary parameters used to define the Jacobian and solve the transport equation for geometric spreading has been summarized in previous ray tracing analyses and is utilized here to compute the Jacobian needed to solve the Burger's equation for the waveform (Blom & Waxler, 2017; Blom, 2019). Thermo-viscous losses are included in this analysis using the Sutherland & Bass model, and are required for stability of the solver as such losses act as a damping factor for the non-linearly generated high frequency energy in the rarefied upper atmosphere (Sutherland & Bass, 2004).

The scaled overpressure is related to the physical overpressure waveform by,

$$u\left(s,\tau\right)=\frac{p\left(s,\tau\right)}{p_{\text{ref}}}\sqrt{\frac{\rho_0 c_0^3\psi_0}{\rho c^3\psi}\frac{c_g D}{c_{g,0}D_0}}. \tag{2c}$$

Note that at $s=s_0$, this reduces to $u\left(s_0,\tau\right)=\frac{p(s_0,\tau)}{p_{\text{ref}}}$ so that p_{ref} is typically defined as the maximum absolute overpressure of the initial waveform. Caustics along the propagation path introduce phase shifts in the waveform that can be accounted for as discussed by Lonzaga et al. (2015); although, unlike the numerical method discussed therein, a Heun's method solver has been implemented for the analysis discussed here and is summarized in Appendix I.

III. Characteristics of Thermospheric Propagation Paths

A broad overview of thermospheric infrasonic signals will be developed using a polynomial fit to the US Standard atmosphere (NOAA, 1976; Lingevitch et al., 1999). The temperature, density, and pressure for this model are shown in the left and right panels of Fig. 1. It should be noted

111 that the parameterized atmosphere only specifies temperature and density, so that pressure is
112 derived by the ideal gas law, $p = \rho RT$, where $R = 287.0\,\frac{\mathrm{J}}{\mathrm{kg}K}$ is the specific gas constant. Simple,
113 qualitative wind models are added to the US Standard atmosphere to describe tropospheric and
114 stratospheric wind jets (also termed the jet stream and circumpolar vortex, respectively) as well
115 as atmospheric tides that become significant in the meso- and thermosphere (Chapman &
116 Lindzen, 2012). The tropospheric and stratospheric winds are defined as,

$$u_{\mathrm{jet}}(z) = V_0 \sin\theta_0\, e^{-\frac{1}{2}\left(\frac{z-z_0}{\sigma_0}\right)^2}, \tag{3a}$$

117

$$v_{\mathrm{jet}}(z) = V_0 \cos\theta_0\, e^{-\frac{1}{2}\left(\frac{z-z_0}{\sigma_0}\right)^2}, \tag{3b}$$

118 where V_0 is the maximum jet speed, θ_0 denotes the direction of the jet relative to north, z_0 is the
119 altitude of the center of the jet, and σ_0 specifies the width of the jet. Values of these parameters
120 for the atmospheric model shown in Fig. 1 are summarized in Tbl. 1. The atmospheric tides are
121 included using a simple model consisting of a smoothed step function above the stratopause using
122 a characteristic oscillation scale, k_0,

$$u_{\mathrm{tides}}(z) = V_0 \frac{\sin(k_0 z)}{1 + e^{-\frac{z-z_0}{\sigma_0}}}, \tag{4a}$$

123

$$v_{\mathrm{tides}}(z) = V_0 \frac{\cos(k_0 z)}{1 + e^{-\frac{z-z_0}{\sigma_0}}}. \tag{4b}$$

124 In this atmospheric tide model V_0 is again the maximum wind speed, z_0 and σ_0 are the altitude
125 and width of the tides onset and k_0 controls the vertical scale of tidal oscillations. Parameters for

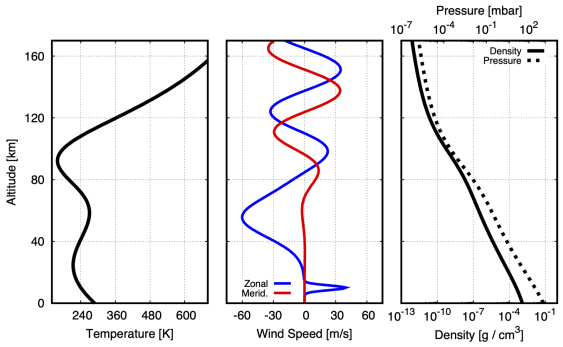

Figure 1: The US Standard atmosphere with a stratospheric jet oriented to the west and atmospheric tides in the meso- and thermosphere.

	V_0	z_0	σ_0	θ_0	k_0
Trop. Jet	40 m/s	10 km	1.5 km	90.0^o	–
Strat. Jet	60 m/s	55 km	12.5 km	-90.0^o	–
Tides	-35 m/s	90 km	12.5 km	–	0.114 km^{-1}

Table 1: Coefficients for the wind models in Fig. 1 as specified by Eqs. (3) and (4)

the model shown in Fig. 1 are included in Tbl. 1. The total zonal and meridional winds, $u(z)$ and $v(z)$, are the sum of the three components and the resulting wind fields are shown in the middle panel of Fig. 1 where the red and blue curves denote the zonal and meridional winds, respectively.

A. Variability due to arrival range and azimuth

Propagation paths have been computed for each of the four cardinal compass directions as well as without the wind included in the US Standard atmosphere model and are shown in Fig. 2. The propagation effects in the upper row are symmetric because the wind has been neglected so

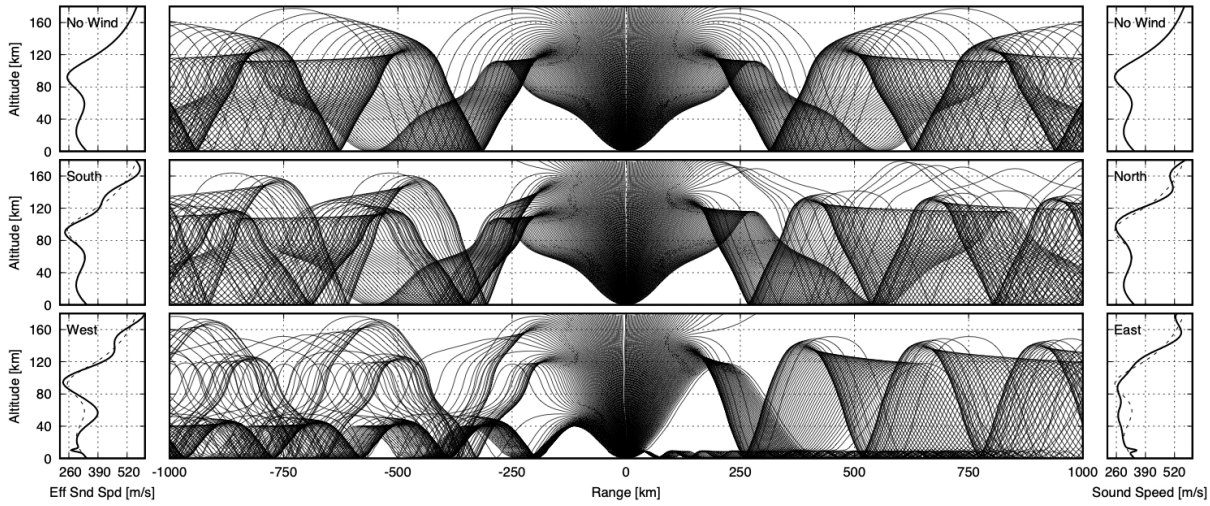

Figure 2: Propagation predictions through the US Standard atmosphere for cases without winds, along the north/south plane, and along the east/west plane show variable interaction with the atmospheric tides and unique propagation effects for returns from the thermosphere.

there is no up- or down-wind direction. The eastward and westward propagation azimuths include arrivals refracted by lower atmosphere wave guides; though, these returns are only present for downwind propagation of the tropospheric and stratospheric wind structures to the east and west, respectively. Properly modeling the coupling of energy in these lower altitude wave guides to that in the meso- and thermosphere can be challenging due to energy leaking between ducts and lead to inaccurate estimates of transmission loss and other complications (Waxler et al., 2017; Waxler & Assink, 2019); though, for the analysis here, propagation effects are computed via application of ray tracing so that these wave guides simply refract shallower ray paths back towards the ground before they enter the middle- and upper atmosphere. While the interaction of the

tropospheric and stratospheric wave guides with the thermospheric waveguide is of interest to a full characterization of infrasonic propagation, the discussion here is focused on only the thermospheric returns so that propagation paths to the east and west in this model will be neglected and further analysis will focus on those paths predicted without winds and to the north and south.

The northward and southward propagation directions exhibit variable turning heights for thermospheric returns due to the atmospheric tides and, in the case of southward propagation, the thermospheric wave guide separates into two distinct turning heights at approximately 110 and 150 km altitude. The northward propagation azimuth is dominated by a wave guide with turning heights at approximately 120 km altitude but the upper atmospheric tides produce a separate set of arrivals refracted at about 170 km for which geometric spreading is increased due to the relatively narrow width of the wind maximum.

The initial launch inclination, reduced travel time, and arrival range for direct thermospheric returns to the north and south, as well as without winds, are shown in Fig. 3. In the figure, the black curves denote those predictions without accounting for the atmospheric winds and result in a pair of arrivals, one fast and one slow, similar to those predicted in the stratospheric wave guide (Waxler et al., 2015). The shallower slow arrival corresponds to a propagation path with a lower altitude turning height, while the high inclination angles propagate through fast sound speed and typically arrive before the slow phase. Investigation of the arrival time predictions for all three scenarios reveals similar phase reversals near the edge of the ensonified region as previously

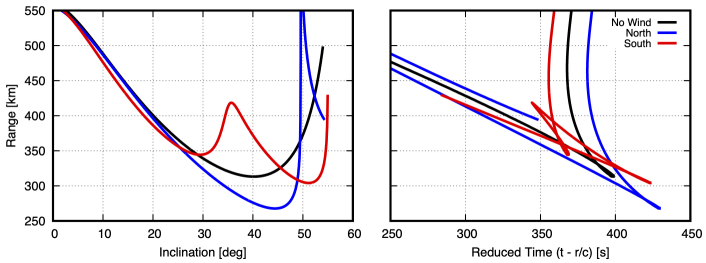

Figure 3: Ray path initial inclination angle, arrival range and reduced propagation time for thermospheric infrasound signals to the north and south compared with those predicted without winds.

discussed for stratospheric propagation when considering spherical geometry. The increased turning height of thermospheric propagation paths produces more notable reversals, extending nearly 20 km spatially and exhibiting a more than 2 second reversal of the arrival times compared with 10 – 12 kilometer spatial extent and 0.5 – 1.0 second reversal for the stratospheric pair. See Blom (2019) for a full discussion of such phase reversals.

When including the winds in the northward and southward propagation cases, the additional refraction by the atmospheric tides complicates this simple arrival pair leading to the more complicated set of paths shown in the blue and red curves for propagation to the north and south, respectively. Because of the added refraction of the winds, some propagation ranges are expected to receive as many as four distinct geometric arrival phases (e.g., 350 – 425 km south of the source). It can be assumed that over the short time and distance in which the separate signals overlap near the ground, the non-linear interaction between the different phases is small. Thus, the total waveform at a given receiver location can be obtained by simply summing over the eigenpaths from the origin to the receiver. In these cases, the thermospheric arrival separates into

two fast and slow phase pairs associated with the refraction altitudes of 110 and 150 km as mentioned previously. Similarly to the phase reversal near the edge of the ensonified region, the duration of the arrivals and overlap of the individual waveform contributions is likely to make resolving the various phases a challenge in infrasonic data.

The weakly non-linear waveform predictions for the windless, southward, and northward propagation cases are shown in Fig. 4 as the black, red, and blue curves, respectively. The upper panels of the figure show the source waveform used to initialize the Burger's equation solver which is an overpressure record captured 7.4 km from a 45 ton surface explosion. In the left column, the Sutherland & Bass losses are included in the prediction, while on the right those losses are scaled down (but still sufficiently strong to provide numerical stability) in order to visualize any waveform contributions with low amplitude attributable to the increased absorption losses at high altitude. That is, the difference between the left and right columns is due to absorption losses and not to non-linear or geometric spreading losses. A detail of the predicted arrivals at 410 km is shown in Fig. 5.

It should be noted that the source impulse exhibits a dominant frequency of approximately 1 Hz, while the thermospheric arrivals have peak frequency content on the order of 0.08 Hz and lower due to the finite amplitude waveform stretching. In the upper right panel, the fast and slow phases of the thermospheric pair are visible for the windless case; however, including the Sutherland & Bass losses leads to the fast arrival phase being markedly lower amplitude than the slow phase and the dominant contribution to the predicted waveform is the slow arrival phase.

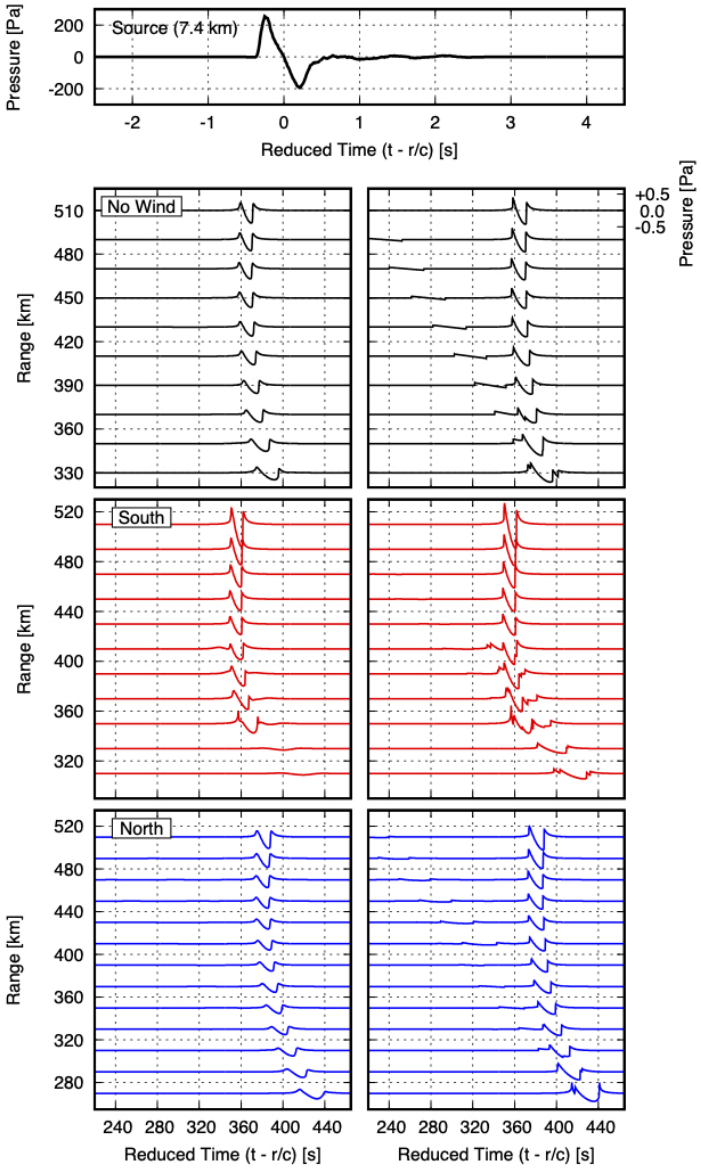

Figure 4: Predicted thermospheric arrival waveforms to the north (lower panel, blue) and south (middle panel, red) of an explosive source compared to those predicted without accounting for winds (upper panel, black). A overpressure record 7.4 km from a surface explosion is used as the source waveform for prediction. The left column includes absorption losses as defined by Sutherland & Bass while the right columns does not include these losses.

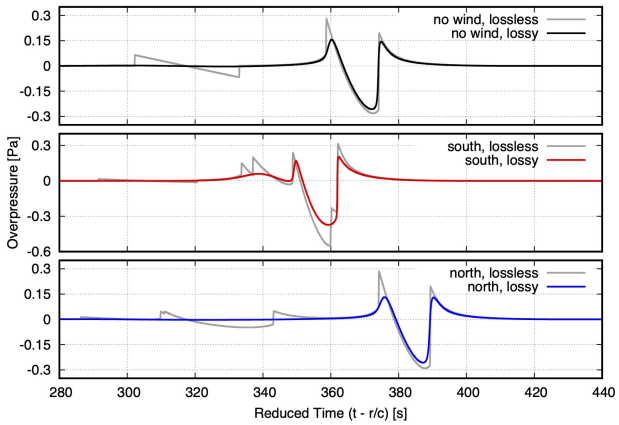

Figure 5: Detail of the waveforms in Fig. 4 at 410 km range: predicted thermospheric arrival waveforms to the north (lower panel, blue) and south (middle panel, red) of an explosive source compared to those predicted without accounting for winds (upper panel, black) 410 km from the source. A overpressure record 7.4 km from a surface explosion is used as the source waveform for prediction. The the waveforms without absorption losses are overlayed in grey.

The amplitude of the fast arrival phase is small even in the lossless case due to the waveform stretching associated with the higher turning point of the fast arrival propagation path (i.e., the fast arrival is lower frequency than the slow arrival due to increased stretching in the more rarefied higher atmosphere and is therefore also lower amplitude due to conservation of energy in the waveform stretching), and is too small to be seen when attenuation is included.

For the southward and northward propagation cases, the more complicated multi-pathing results in more complicated waveform predictions, but with very low amplitude for all phases except the slow arrival phase. This is due to more intense absorption at increased turning heights and the losses due to large waveform stretching. Notably, the nearer pair of arrivals in the

205 southward propagation direction are predicted to be very low amplitude due to the absorption
206 losses. In the right column of Fig. 4, the arrivals between 310 and 350 km south of the source are
207 predicted to arrive at later reduced time and exhibit lower frequency content; however, in the left
208 column predictions, including absorption losses, these arrivals are very low amplitude due to these
209 losses and potentially below typical noise levels. This behavior is seen clearly in Fig. 5 where a
210 detail of the arrival at 410 km is shown. Comparing these predictions with the range-inclination
211 relations in Figs. 2 and 3, one finds that these shorter range arrivals correspond to those paths
212 with initial inclination angles of $35 - 55^o$ and propagation paths with turning heights of 130 – 150
213 km where as the arrivals predicted to be higher amplitude correspond to those paths with
214 inclinations of $0 - 35^o$ and turning heights on the order of 90 – 110 km.

215 Given the severe attenuation in the thermosphere, it has appeared somewhat mysterious that
216 thermospheric phases are observed at all. Lonzaga et al. (2015) showed that the period
217 lengthening that a pulse undergoes in the thermosphere shifts the pulse spectrum to lower and
218 lower frequencies, making attenuation relatively insignificant. Here, we see that this picture is too
219 simple. It appears to be generally true for the slow thermospheric arrival, but the fast arrivals
220 propagate higher into the thermosphere where a combination of more severe attenuation and
221 period lengthening seems to render their signal amplitudes too small to be easily observed in
222 typical noise conditions.

223 In summary, for infrasonic signal propagation in the thermosphere the strong impact of
224 non-linear propagation effects on the waveform structure results in a much lower frequency signal

than was produced by the source. Predictions for propagation paths ignoring atmospheric winds produce an arrival pair similar to that expected in the stratospheric waveguide due to the upward refracting lower atmosphere and thermal gradient in the meso- and thermosphere. However, in addition to the geometric spreading losses that lead to a lower amplitude stratospheric fast arrival, thermospheric fast arrival phases undergo waveform stretching and absorption losses that result in an arrival waveform dominated by the slow arrival phase. Including more realistic winds in the meso- and thermosphere produces more complex propagation effects exhibiting increased multi-pathing; though, these additional arrivals often refract from increasing altitude and so undergo similar losses as the fast arrival in the windless case. Thus, thermospheric signals from an explosion or similar impulsive source are expected to consist of a relatively shallow inclination, high amplitude, low frequency u-wave that is the Hilbert transform of the impulse after it has shocked into an N-wave and been stretched in the rarefied upper atmosphere. The signal may include several steeper inclination, lower amplitude arrivals that are typically even lower frequency than the dominant phase due to enhanced non-linear propagation effects for higher turning heights, but may only be observable at locations near the edge of the ensonified region due to the excessive absorption and non-linear losses at increased altitude.

B. Coincident arrivals from multiple paths

Although the general conclusion of the previous section are valid is the vast majority of cases, it is worth more closely examining the multi-pathed arrivals in a number of scenarios. The tidal wind contributions in Eq. (4) can be modified to include a phasing factor, $k_0 z \to k_0 z + \varphi$.

Adjusting this phasing factor shifts the altitude at which the inflection in the sound speed for southward propagation occurs in Fig. 2. In Fig. 6, phase shifts of $\pm 30^o$ and $\pm 10^o$ are used to produce the four effective sound speed profiles in the left panel. The central panel shows the arrival range and launch inclination for these atmospheric models and the set of panels on the right show the arrival waveforms predicted at ranges of 330 to 500 km. The spatial extent of the multi-pathing is strongly dependent on the inflection characteristics and the lower altitude inflections are found to produce more notable changes in the arrival waveform and deviations from the u-wave that is seen for the simpler single thermospheric slow arrival. The strongest deviations from the canonical u-wave occur when near the edges of ensonification where a caustic is located at the ground surface similar to that found for stratospheric propagation (Waxler et al., 2015); therefore, some caution should be taken in accepting these predicted waveforms produced by multi-pathing near sound speed inflections and the canonical form discussed in the previous section can be expected to be representative for most thermospheric propagation. Additional modeling using finite frequency methods including the weak shock effects is needed to fully understand the arrival near the caustic at the ground surface; though, such analysis is beyond the scope of the work presented here.

C. Variations in the near-source waveform

The infrasonic signals observed some distance from a source are determined by a combination of the overpressure waveform produced by the source and the influence of propagation as the signal travels from the source to the receivers. The detection of such signals is

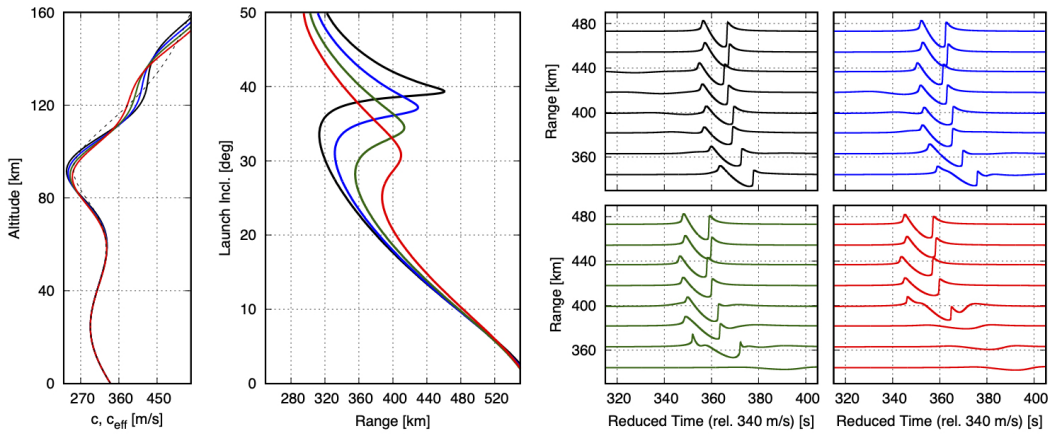

Figure 6: Phase shifts in the atmospheric tides produce shifts in the inflection of the sound speed (left). The resulting arrival characteristics show multi-pathing covering varying spatial extents (center) and comparison of the various waveform predictions show that in many cases the canonical u-wave arrival is predicted; though, in the case of lower altitude inflections, additional contributions produce a more complex waveform structure.

dependent not only on these source and propagation effects, but also on the ambient noise conditions at the array within the frequency band in which the signal contains energy. In the previous section it was shown that the shallow inclination, "slow" arrival phase of the thermospheric pair typically dominates the arrival waveform due to the excessive absorption and non-linear losses for propagation paths at higher inclination angles. However, this analysis presumed a specific, impulsive acoustic source shown in the upper panel of Fig. 4, while transient infrasonic sources can produce a variety of near-source pressure signatures. Because of this, in addition to understanding how propagation at various ranges through the atmosphere impacts the resulting infrasonic signal, understanding what characteristics of the near-source reference waveform can be recovered in the propagated thermospheric arrival is crucial in efforts to develop

methods aimed at using thermospheric arrivals to characterize an infrasonic source.

Consider the eigenray path shown in the upper panel of Fig. 7 connecting a surface infrasonic source to a receiver 325 km to the north through the model atmosphere shown in Fig. 1. The lower left and right panels show near-source waveforms and the resulting thermospheric arrival, respectively. A classical blastwave overpressure record is shown in black, a lower frequency acoustic impulse is shown in blue, and a u-wave source is shown in red. Somewhat surprisingly, the resulting thermospheric arrivals are practically identical for all three sources. In actuality, the frequency content and amplitude of each of the sources was chosen so that the arrival waveforms have approximately the same period and amplitude; however, regardless of these selected amplitudes and frequencies, thermospherically refracted infrasound signals frequently exhibit the u-wave shape shown in Fig. 7 and discussed previously.

The reason for this consistency in thermospheric infrasound waveform characteristics is due to the non-linear propagation of signals in the rarefied upper atmosphere and specifically the waveform stretching that occurs as the maximum over- and under-pressure of the waveform shift forward and backward, respectively (Rogers & Gardner, 1980). Each of the dots along the eigenray shown in Fig. 7 denotes 40 kilometer steps along the path and the red star denotes a caustic encountered shortly after reaching the turning height. The waveform calculated along the ray path is shown in Fig. 8 at the initial point as well as at each of these 40 kilometer steps. As each waveform propagates, it shocks into an N-wave by the time it reaches 120 km along the path (comparison with Fig. 7 shows this ray length corresponds to approximately 75 km altitude).

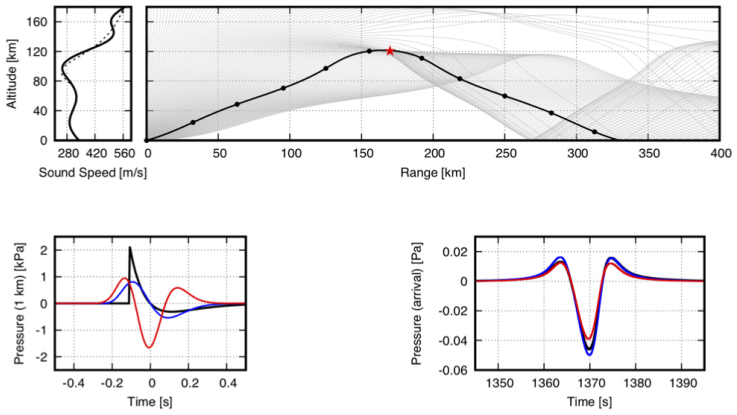

Figure 7: Predicted thermospheric arrival waveforms for an explosive blast wave (black), acoustic impulse (blue), and u-wave (red) along a given propagation path. The points along the propagation path denote 40 km ray length increments and the star denotes the location of a caustic.

This N-wave elongates as it propagates through the rarefied upper atmosphere that requires the change to a longer time scale for the upper set of panels in the figure. Much of the high frequency energy is lost due to absorption, so that the shock components of the waveforms are lost. Following passage through the caustic between 200 and 240 km, the impulse undergoes a 90^o phase shift (i.e., a Hilbert transform) and travels back to the ground as a u-wave. In summary, the ray tracing and weakly non-linear propagation analysis utilized here predicts that thermospheric infrasound signals will exhibit a characteristic u-wave shape as a result of non-linear propagation effects. These cause the source waveform to shock into an N-wave during propagation from the ground up to the thermosphere regardless of its initial shape. In the thermosphere, much of the high frequency content in the waveform is lost and the long duration impulse then passes through

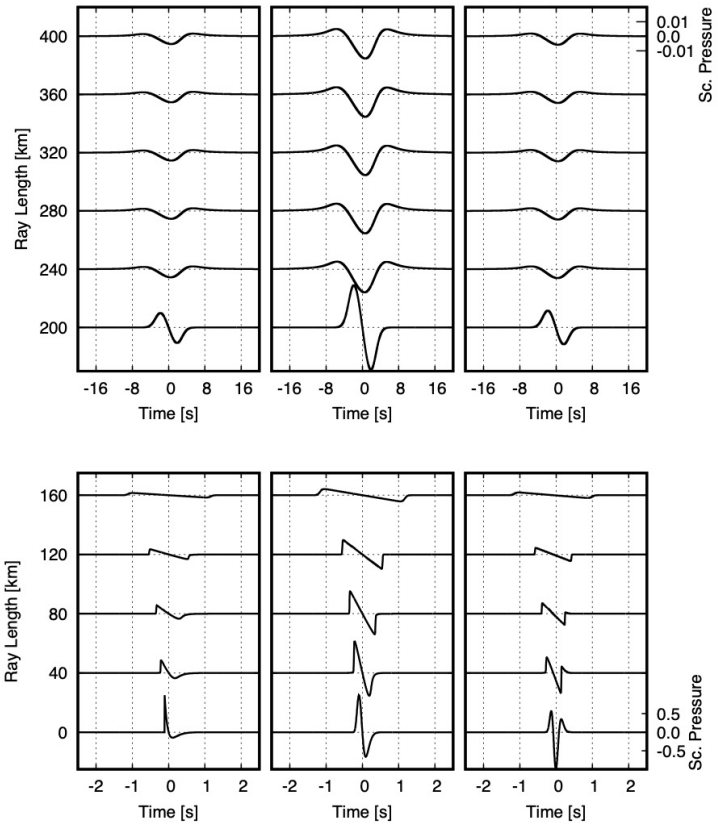

Figure 8: Evolution of waveforms along the eigenray path for the propagation path and near-source waveforms shown in Fig. 7. The lower and upper panels have different time and pressure scales.

a caustic, producing in a phase shift of the impulse into the u-wave shape, before returning to the ground surface. This occurs regardless of the details of the initial waveform shape.

Although the persistent u-wave shape of thermospheric infrasound appears to limit characterization of the source, comparison of predicted waveforms from a similar source model with varying amplitude and time scale produces a corresponding variation in the resulting thermospheric arrival. Consider the blastwave source models shown in Fig. 9 along the same

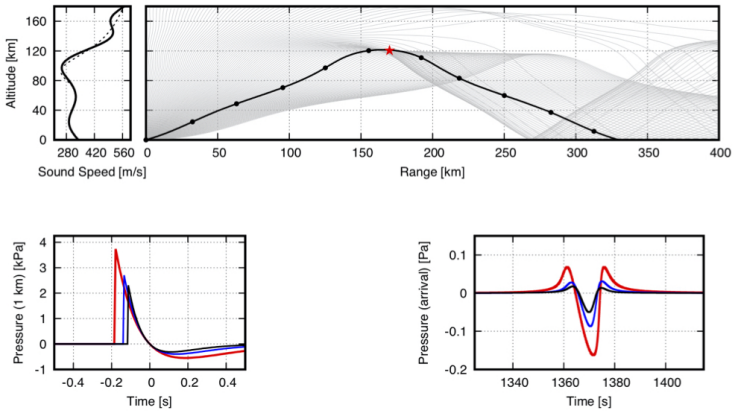

Figure 9: Predicted thermospheric arrival waveforms for explosive blast waves predicted for blasts of 10 (black), 20 (blue), and 50 (red) tons. As in Fig. 7, the points along the propagation path denote 40 km ray length increments and the star denotes the location of a caustic.

propagation path as in Fig. 7. In this case, the Kinney & Graham predicted overpressure and positive phase duration values have been used to predict blastwaves corresponding to 10, 20, and 50 ton equivalent TNT chemical explosions on the ground surface shown as the black, blue, and red waveforms, respectively (Kinney & Graham, 1985). The arrival waveforms in this case exhibit increasing amplitude with larger explosive yield as expected, and the dominant frequency of the u-wave is found to decrease with larger yield. The initial positive phase durations of 0.11, 0.14, and 0.19 seconds produce signals with peak-to-peak times of 10.5, 12.0, and 13.5 seconds.

Samples of the propagating waveforms for the 10, 20, and 50 ton explosive blastwaves in Fig. 9 are shown in the left, center, and right columns of Fig. 10, respectively, again showing the waveform predicted every 40 km along the propagation path. As in the previous analysis with

varying source waveforms, the infrasonic signals shock into N-waves by the 120 km ray length; however, the higher amplitude sources already exhibit increased pulse lengthening even at this short distance. Once again, propagation into the upper atmosphere results in absorption losses for high frequency content in the signals, and the caustic encounter introduces a phase shift changing the impulse into a u-wave. Note that once the waveform changes into this shape, there is no longer any pulse broadening as the first and second peaks move forward together; however, the negative phase moves backward producing asymmetry in the u-wave. Though not shown in the figure, repeating this analysis with blastwaves of initially identical overpressure, but varying positive phase duration, produces arrivals with practically identical peak-to-peak times. However, blastwaves of initially identical positive phase duration, but varying initial overpressure, produces distinct peak-to-peak times for the resulting thermospheric signals. This leads to the conclusion previous identified by other analyses that the peak-to-peak time or dominant frequency of a thermospheric infrasonic signal might be used to infer information about the source amplitude and therefore the source's energy content (i.e, explosive yield) (Kulichkov, 2002; Assink et al., 2013; Lonzaga et al., 2015)

D. Variability in the atmosphere and eigenray path

Utilizing thermospheric infrasonic signals for source characterization is complicated not only by the spatial variability of arrivals, but also by the temporal variability and sparse measurements of the atmosphere and the inherent uncertainty in the acoustic propagation medium. As discussed in a number of other analyses (Kulichkov et al., 2010; Drob et al., 2013, 2010a; Lalande & Waxler,

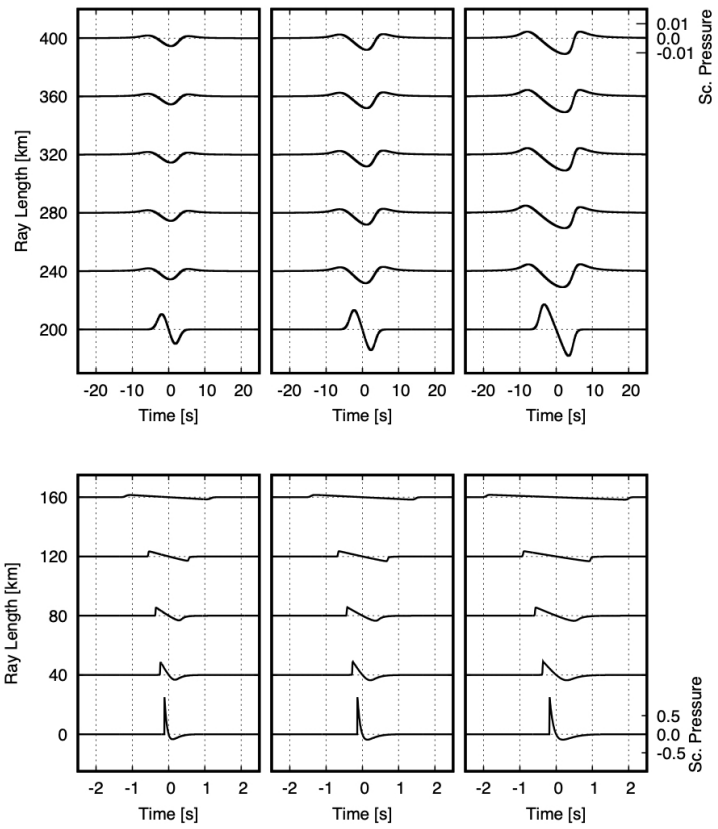

Figure 10: Evolution of waveforms along the eigenray path for the propagation path and near-source waveforms shown in Fig. 9. As in Fig. 8, the lower and upper panels have different time and pressure scales.

2016; Assink et al., 2019), uncertainty in the atmospheric state produces a corresponding uncertainty in infrasonic propagation effects which can limit the confidence in localization and source characterization estimates. Thus, in addition to the spatial and source-related variations in predicted thermospheric signals discussed in the previous sections, temporal variability in the atmosphere is expected to produce variations in the eigenray solutions even for a fixed source-receiver geometry so that observed infrasonic signals from a repeating source observed at the same receiver location will vary from event to event.

Leveraging historically archived atmospheric specifications from the Ground-to-Space (G2S) tool (Drob, 2019), the variability in thermospheric infrasound can be quantified using an approach similar to that used in constructing propagation-based, stochastic models for path geometry or transmission loss in which a large suite of atmospheric states are considered and the variability of propagation results is quantified in a statistical framework (Blom et al., 2015, 2018). G2S atmospheric specifications for the month of January during 2007 are shown in Fig. 11 along with the eigenray predictions for a receiver 350 km north of a source. The G2S archived atmospheric data used here is sampled four times per day, producing six-hour resolution of the atmospheric state over the course of the month and more than 120 individual specifications to consider. Note that, although numerical weather prediction information is utilized in defining the lower- and mid-altitude layers of the G2S specification, the meso- and thermospheric regions are defined via climatology models and do not exhibit as much variability in specifications. Because of this, the estimated variability of thermospheric infrasound using this suite of atmospheres from

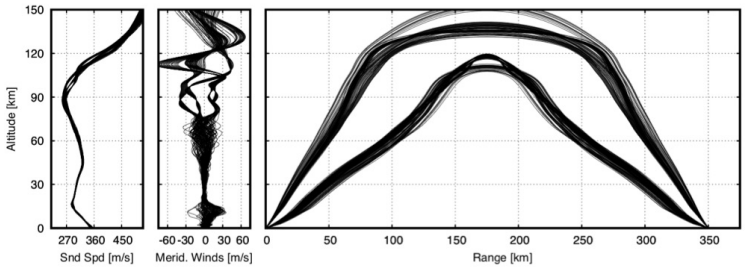

Figure 11: Variability of the atmospheric structure through January, 2007 in the western US as specified by the G2S archive (left). The predicted eigenrays from a source to a receiver 350 km to the north using the archived G2S specifications (right).

a single month and year is likely an underestimate of the overall variability. Eigenrays have been computed for both the fast and slow branches of the thermospheric pair as shown in the figure by extending the search to inclination angles up to 60^o and contributions from each are combined into a single arrival waveform for continued analysis.

Although time-domain waveform predictions have been computed for each atmospheric state in the analysis suite, a frequency domain analysis is more informative for characterizing how variation in the source and atmosphere couple together as discussed previously for source characterization using tropo- and stratospheric infrasonic signals (Blom et al., 2018). The explosive blastwaves in the Kinney-Graham model corresponding to 10, 20, and 50 ton yields shown in the lower left panel of Fig. 9 have been used as sources for the suite of eigenray solutions in Fig. 11. The near-source spectral amplitudes for these three sources are shown in the left panel of Fig. 12 while the arrival spectral amplitudes for this suite of atmospheres are shown in the right three panels of the figure. The overall amplitude of the spectrum decreases as one would expect

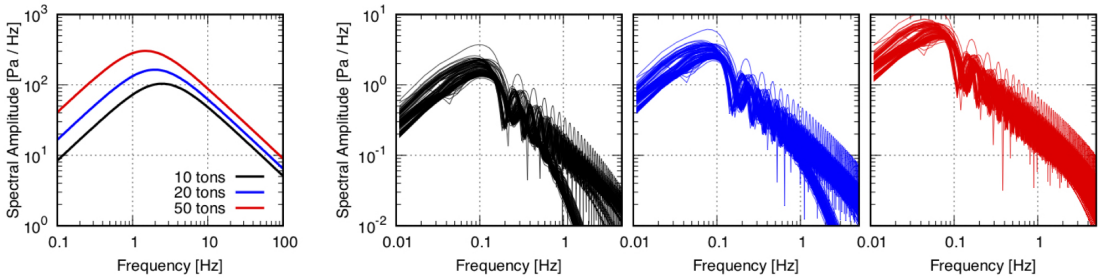

Figure 12: Predicted variability in the thermospheric arrival spectral amplitude for explosions with yields of 10, 20, and 50 tons for the archived G2S specifications in Fig. 11. The near source (1 km) blast wave spectra using the frequency domain blast wave model discussed in Blom et al. (2018) are shown in the left panel for all three explosions and the resulting scatter of arrival spectra are shown on the right. Throughout black, blue, or red lines indicate 10, 20, or 50 tons, respectively.

for propagation due to a combination of geometric spreading and absorption, but the dominant frequency of the source and arrival spectra change by a significant amount due to the combined non-linear propagation effects broadening the pulse and the loss of high frequency energy due to absorption. This leads to sources with peaks on the order of 1 – 2 Hz producing thermospheric arrivals 350 km away with dominant frequencies covering a range from 0.05 to 0.12 Hz.

The predicted thermospheric arrivals in Fig. 12 have been further analyzed to identify the dominant frequency of each. These frequencies have then been used to construct kernel density estimates (KDEs) approximating the distributions of dominant frequencies of arrivals from 10, 20, and 50 ton sources at this location. The resulting distributions for dominant frequency of the thermospheric arrival are shown in Fig. 13. In the figure, the 10 and 20 ton distributions are found to overlap by some degree, indicating that as it is possible for thermospheric signals

produced by the 10 and 20 ton surface explosions to exhibit identical dominant frequencies so that such an observation may be unable to distinguish between the two sources. Further, comparing the spectra of the predicted thermospheric arrivals for the 10 and 20 ton sources in Fig. 12 shows that the amplitudes of the arrivals produced by two sources overlap by a significant amount so that combining analysis of dominant frequency with the overall signal amplitude may not provide additional separation of the two source yields. Similar analysis of the 20 and 50 ton predictions, however, shows strong separation between the two so that an observed thermospheric return from an explosion with dominant frequency of 0.06 Hz is likely to be a source with yield on the order of 50 tons and highly unlikely to be a 10 or 20 ton source. Developing an inversion capability for estimating explosive yield with quantified uncertainty using thermospheric infrasonic signals is beyond the scope of this discussion; however, the methodology discussed here provides a justification and expectation that such a methodology could provide accurate and precise estimates of explosive yield. Additionally, combination of such a method with existing infrasonic yield estimation methods that leverage tropospheric and stratospheric arrivals would be a path towards development of a robust infrasonic source characterization capability.

IV. Comparisons to recently published analysis of thermospheric signatures from surface explosions

The aim of the theoretical analysis presented here is to provide a framework for analyzing data and thermospheric signals. Two specific data sets, previously presented in the literature, will be discussed to demonstrate the insights gained from these analyses. These are the thermospheric

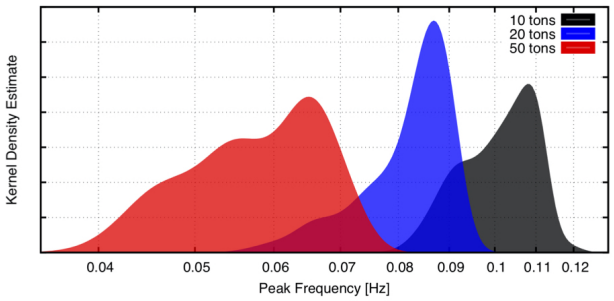

Figure 13: Distributions of peak frequency for the spectra in Fig. 12 show some overlap indicating a non-negligible amount of uncertainty in an estimated yield derived from thermospheric arrival characteristics.

returns detected on the US Transportable Array (TA), from the October 28, 2014 Antares Rocket detonation at Wallops Island, Virginia (Vergoz et al., 2019) and observations from the Humming Roadrunner (HRR) exercise (Green et al., 2018). In this paper only a cursory, qualitative discussion of data will be undertaken and it should be noted that the atmospheric specifications in the upper atmosphere are rarely sufficient to accurately model signal propagation (Assink et al., 2013, 2019). This is likely due to several factors including the large scale spatial and temporal interpolations required, and the lack of contemporaneous data to constrain the model. Thus, unless some atmospheric updates are included, any predictions are, to some degree, qualitative in nature. It is likely that, to obtain reasonable quantitative agreement will require atmospheric updating that goes beyond the scope of the current work (Assink et al., 2013; Lonzaga et al., 2015; Assink et al., 2019). In addition, the dependence here on the geometrical acoustic approximation can lead to error as noted in discussion of the multi-pathing produced by inflections of the effective sound speed.

418 The Wallops Island event occurred as a rocket launch at the Wallops Island Flight Facility
419 failed, leading to the rocket's detonation. The resulting blast wave propagated efficiently through
420 the atmosphere and was detected on the TA at distances of more than 1000 km from the event
421 location. The event and the TA are described in the Vergoz et al. (2019) monograph. Among the
422 reported observations are many thermospheric phases, including thermospheric phases with
423 multiple ground bounces. Geometrical acoustics was used to analyze the observations and, as
424 expected, results are mostly qualitative, requiring some physically reasonable, yet mathematically
425 unjustified, extensions (see section 9.3.2 of Vergoz et al. (2019)). A sample of some waveforms of
426 single ground bounce thermospheric phases is shown in Fig. 9.8 of Vergoz et al. (2019), and some
427 of the waveforms show the expected u-wave shape while others are more complex, potentially
428 produced by multi-phase superposition as described in Sec. III.B above. Indeed, the atmospheric
429 profiles presented in Vergoz et al. (2019) in their Fig. 9.2 have the required thermospheric
430 undulations to produce inflections in the effective sound speed profile and multi-pathing. More
431 analysis is required to test this hypothesis and potentially model observed waveforms.

432 The Humming Roadrunner exercise was performed by the US Defense Threat Reduction
433 Agency (DTRA) and consisted of a series of large, controlled chemical explosions at various
434 locations on the White Sands Missile Range (WSMR). The experiment and the far field
435 infrasound array deployments are described in Green et al. (2018). Here, thermospheric signals
436 received to the north on three arrays, N300, N340 and N380, will be discussed in detail. The
437 numbers are nominally the range to the explosion locations from the three source locations used

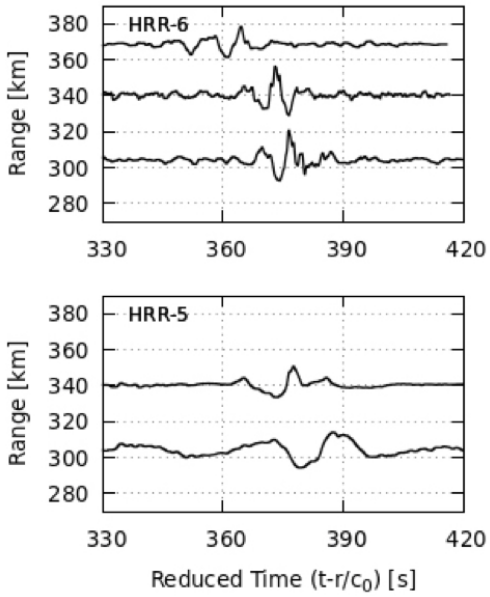

Figure 14: Observed infrasonic signals for the northern line of arrays deployed during the Humming Roadrunner experiment exhibit arrivals consistent with thermospheric propagation paths.

in the exercise. Only the last two, nominally 45 ton, explosions produced clear thermospheric phases on these arrays. These are referred to as HRR-5 and HRR-6 and the best beam waveforms are plotted in Fig. 14 as functions of reduced time in order to more directly compare the arrivals across the three locations. The HRR-5 arrivals are roughly u-wave shaped while the HRR-6 waveforms are more complex and higher frequency; though, they also contain distinct u-wave forms. The reduced time at which energy arrives at each of the arrays decreases with range as predicted for the slow arrival branch of a thermospheric pair.

The arrival trace velocity, celerity, and dominant frequency content for each arrival has been computed and are summarized in Tbl 2. Unlike the observations of the Wallops Island event on

		N300	N340	N380
HRR-5	Trace Vel.	420 m/s	370 m/s	–
	Celerity	238 m/s	248 m/s	–
	Dominant Freq.	0.048 Hz	0.046 Hz	–
HRR-6	Trace Vel.	365 m/s	355 m/s	345 m/s
	Celerity	240 m/s	248 m/s	254 m/s
	Dominant Freq.	0.13 Hz	0.14 Hz	0.12 Hz

Table 2: Trace velocity, celerity (horizontal group velocity), and dominant frequency for thermospheric arrivals observed during the Humming Roadrunner experiment. For reference, the Kinney & Graham scaling law predictions for the near-source dominant frequency of 45 ton surface explosion is on the order of 0.84 Hz.

the TA, the arrays utilized in analysis of the HRR events allow for beam analysis and estimation of the arrival inclination angle via the trace velocity. In agreement with the expected characteristics of the thermospheric slow branch, trace velocities decrease with range as the shallower propagation paths arrive further from the source and increased inclination angles shift arrivals towards the near edge of the ensonified region. As noted above, the reduced time of the arrivals is earlier for the arrays further from the source, and the celerities of the arrivals follows this trend in that those arrivals further from the source exhibit faster celerities. Thus, the spatial trends predicted from the ray tracing analysis are observed in this data set in that trace velocities of thermospheric arrivals decrease with range while celerities increase.

Lastly, the observed peak frequencies of the HRR-5 versus -6 phases are notably different

457 from one another, despite the source strengths and locations being nearly identical. The peak
458 frequency of the HRR-5 phase arrivals is in the expected range predicted in Fig. 13, while that of
459 HRR-6 is notably higher and doesn't fall within the predicted range of values. A likely
460 explanation for this discrepancy can be identified by comparing the arrival trace velocities for the
461 two events. At N300, the observed trace velocities correspond to inclination angles on the order of
462 35^o and 20^o for HRR-5 and -6, respectively (assuming a sound speed at the ground of 340 m/s).
463 The steeper arrival inclination during HRR-5 implies that the turning height of the propagation
464 paths for that event is markedly higher than that for HRR-6, which would explain the differences
465 in dominant frequency as propagation paths extending to higher altitude pass through regions of
466 lower density and undergo more severe non-linear propagation effects. Comparing the observed
467 dominant frequencies with those in Fig. 13, it is likely that the propagation paths for HRR-5 are
468 relatively well described by the specifications in the G2S archive; however, the propagation paths
469 for HRR-6 exhibit lower altitude turning heights potentially due to the presence of gravity
470 (buoyancy) waves in the middle- and upper-atmosphere not included in the G2S specifications.
471 Again, specifications in the upper atmosphere are typically not accurate enough to forward model
472 propagation (Assink et al., 2013, 2019), and the results here imply that updates to the
473 atmospheric state should leverage not only the travel times from source to receiver but also the
474 inclination angle of the incident signal via the trace velocity. Regardless, observed trends in the
475 arrival characteristics of thermospheric propagation paths are in agreement with predictions
476 obtained using a combination of ray tracing and weak shock theory so that many features of such

observations can be understood and explained.

V. Conclusions

In many cases, infrasonic signals propagate into the middle- and upper atmosphere where the decreased ambient density results in finite amplitude, non-linear propagation effects. Modeling the propagation along such paths has been completed here using a combination of acoustic ray tracing to identify propagation path geometry and travel time coupled with a weakly non-linear solution of the transport equation that predicts the waveform evolution in the weak shock limit. A canonical u-wave structure is identified for most scenarios as those paths which are refracted from higher altitudes undergo significantly more attenuation due to thermo-viscous and non-linear losses; although, inflections in the effective sound speed can produce multi-pathing that adds some complexity to the waveform structure. Such complexities are typically spatially localized and dependent on the altitude at which the effective sound speed inflection occurs.

Analysis of thermospheric returns from varying source models has shown that while phase information and waveform complexity near the source is lost due to the finite amplitude effects, there is a strong dependence of the arrival waveform frequency content on the near-source peak overpressure. Combining this analysis with uncertainty quantification using a suite of possible atmospheric states has shown that analysis of thermospheric infrasound may provide additional means of estimating explosive yield with reasonable confidence. Further, it's likely that combining analysis of thermospheric infrasound signals with that using tropospheric and stratospheric signals may provide a robust yield estimation approach for analysis of surface explosions using

497 regional infrasonic observations.

498 Lastly, thermospheric signals from the Wallops Island Antares Rocket detonation that
499 occurred during 2014 as well as observations of large chemical explosions conducted as part of the
500 2012 Humming Roadrunner exercise show qualitative results in agreement with those predicted in
501 that trace velocities decrease with distance from the source while celerities increase. Also,
502 although the pair of events considered from the Humming Roadrunner experiment were identical
503 in explosive yield, the spectral compositions differed significantly. This is likely due to differences
504 in the turning heights which have been identified by comparing observed trace velocities of
505 arrivals for the two explosions. Additional analysis and more robust source and propagation
506 modeling methods are needed to fully understand the characteristics of thermospheric infrasound;
507 however, the combined ray tracing and weak shock analysis conducted here provides a useful set
508 of tools to understand many features of observed signals and identify those signatures that are
509 useful in better relating thermospheric infrasonic returns with the source and propagation path.

510 **Acknowledgements**

511 We gratefully acknowledge the support of Ms. Leslie Casey, Dr. Thomas Kiess, and the
512 National Nuclear Security Administration (NNSA) Office of Defense Nuclear Nonproliferation
513 Research and Development (DNN R&D) for funding the propagation modeling development and
514 implementation. The Humming Roadrunner experiment was conducted by the Defense Threat
515 Reduction Agency (DTRA) and the infrasonic data used in this analysis was collected by the
516 University of Mississippi's National Center for Physical Acoustics (NCPA). This work was

conducted by Los Alamos National Laboratory (LANL) under award number

89233218CNA000001 with the U.S. government.

Appendix

I. Solving Burgers' Equation using Heun's Method

Heun's method provides a means of solving a first order differential equation of the form $\frac{dy}{dt} = f(t, y)$ (Stoer & Bulirsch, 2013). Given an initial value, $y_0 = y(t_0)$, the evolution of y can be derived using the relations,

$$\hat{y}_{n+1} = y_n + \delta f(t_n, y_n) \tag{5a}$$

$$y_{n+1} = y_n + \frac{\delta}{2}\left(f(t_n, y_n) + f(t_{n+1}, \hat{y}_{n+1})\right) \tag{5b}$$

$$t_{n+1} = t_n + \delta \tag{5c}$$

Applying this solution to Eq. (2a), one has a solution of the Burgers' equation defined by,

$$\hat{u}_{n+1} = u_n + \delta\tilde{\beta}_n u_n \frac{\partial u_n}{\partial \tau} \tag{6a}$$

$$u_{n+1} = u_n + \frac{\delta}{2}\left(\tilde{\beta}_n u_n \frac{\partial u_n}{\partial \tau} + \tilde{\beta}_{n+1}\hat{u}_{n+1}\frac{\partial}{\partial \tau}\hat{u}_{n+1}\right) \tag{6b}$$

$$s_{n+1} = s_n + \delta. \tag{6c}$$

Applying the definition of $\hat{u}_{n+1}$ and noting that $g\frac{dg}{dx} = \frac{1}{2}\frac{d}{dx}g^2$, the time-domain solution has the

form,

$$u_{n+1} = u_n + \frac{\delta}{2}\left(\frac{1}{2}\left(\tilde{\beta}_n + \tilde{\beta}_{n+1}\right)\frac{\partial}{\partial\tau}u_n^2 + \delta\frac{\tilde{\beta}_n\tilde{\beta}_{n+1}}{2}\frac{\partial}{\partial\tau}u_n\left(\frac{\partial}{\partial\tau}u_n^2\right) + \delta^2\frac{\tilde{\beta}_n^2\tilde{\beta}_{n+1}}{8}\frac{\partial}{\partial\tau}\left(\frac{\partial}{\partial\tau}u_n^2\right)^2\right) \tag{7}$$

Finally, taking a Fourier transform of this result and noting that $\mathcal{F}\left\{\frac{\partial}{\partial\tau}g(\tau)\right\} = i\omega\mathcal{F}\{g(\tau)\}$, one finds the Heun's method solution of the Burgers' equation,

$$U(s+\delta, f) = U(s,f) + i\pi f\delta\left(\frac{\tilde{\beta}(s) + \tilde{\beta}(s+\delta)}{2}\mathcal{A}(s,f) + \delta\frac{\tilde{\beta}(s)\,\tilde{\beta}(s+\delta)}{2}\mathcal{B}(s,f) + \delta^2\frac{\tilde{\beta}^2(s)\,\tilde{\beta}(s+\delta)}{8}\mathcal{C}(s,f)\right), \tag{8a}$$

$$\mathcal{A}(s,f) = \mathcal{F}\left\{u^2(s,\tau)\right\}, \tag{8b}$$

$$\mathcal{B}(s,f) = \mathcal{F}\left\{u(s,\tau)\left(\frac{\partial}{\partial\tau}u^2(s,\tau)\right)\right\}, \tag{8c}$$

$$\mathcal{C}(s,f) = \mathcal{F}\left\{\left(\frac{\partial}{\partial\tau}u^2(s,\tau)\right)^2\right\}. \tag{8d}$$

where $U(s,f) = \mathcal{F}\{u(s,\tau)\}$.

The implementation of this solution takes a provided waveform, $p(s_1,\tau)$, at some initial location along a ray path, s_1, and defines $u(s_1,\tau)$ as in Eq. (2c). One then utilizes a Fourier transform to obtain $U(s_1,f)$ and finite difference derivatives to define $\frac{\partial}{\partial\tau}u^2(s_1,\tau)$ in order to

compute $U(s_1 + \delta, f)$, which can then be Fourier transformed to obtain $u(s_1 + \delta, \tau)$ and repeated until the location along the ray path of interest, s_2, is reached. The physical acoustic waveform at that point along the ray path is then computed as,

$$p(s, \tau) = u(s, \tau) \times p_{\text{ref}} \sqrt{\frac{\rho c^3 \psi}{\rho_0 c_0^3 \psi_0} \frac{c_{g0} D_0}{c_g D}}. \tag{9}$$

REFERENCES

Assink, J. D., Waxler, R., Frazier, W. G., & Lonzaga, J. (2013). "The estimation of upper atmospheric wind model updates from infrasound data." *Journal of Geophysical Research: Atmospheres*, 118(19), 10-707.

Assink, J., Smets, P., Marcillo, O., Weemstra, C., Lalande, J. M., Waxler, R., & Evers, L. (2019). "Advances in infrasonic remote sensing methods." In *Infrasound Monitoring for Atmospheric Studies* (pp. 605-632). Springer, Cham.

Blom, P. S., Marcillo, O., & Arrowsmith, S. J. (2015). Improved Bayesian infrasonic source localization for regional infrasound. *Geophysical Journal International*, **203**(3), 1682-1693.

Blom, P. & Waxler, R. (2017). "Modeling and observations of an elevated, moving infrasonic source: eigenray methods". *J. Acoust. Soc. Am.*, **141**(4), 2681–2692.

Blom, P. S., Dannemann, F. K., & Marcillo, O. E. (2018). "Bayesian characterization of explosive sources using infrasonic signals." *Geophysical Journal International*, **215**(1), 240-251.

Blom, P. (2019). "Modeling infrasonic propagation through a spherical atmospheric layer—Analysis of the stratospheric pair." *J. Acoust. Soc. Am.*, **145**(4), 2198–2208.

Chapman, S., & Lindzen, R. S. (2012). *Atmospheric tides: thermal and gravitational*. Springer Science & Business Media.

Drob, D. P., Picone, J. M., & Garcés, M. (2003). Global morphology of infrasound propagation. *Journal of Geophysical Research: Atmospheres*, **108**(D21).

Drob, D. P., Meier, R. R., Picone, J. M., & Garcés, M. M. (2010a) "Inversion of infrasound signals for passive atmospheric remote sensing." In *Infrasound monitoring for atmospheric studies* (pp. 701-731). Springer, New York.

Drob, D. P., Garcés, M., Hedlin, M., & Brachet, N. (2010b). "The temporal morphology of infrasound propagation." *Pure and applied geophysics*, **167**(4-5), 437-453.

Drob, D. P., Broutman, D., Hedlin, M. A., Winslow, N. W., & Gibson, R. G. (2013). "A method for specifying atmospheric gravity wavefields for long-range infrasound propagation calculations." *Journal of Geophysical Research: Atmospheres*, **118**(10), 3933-3943.

Drob, D. (2019). "Meteorology, climatology, and upper atmospheric composition for infrasound propagation modeling." In *Infrasound Monitoring for Atmospheric Studies* (pp. 485-508). Springer, Cham.

Evers, L. G., & Haak, H. W. (2007). "Infrasonic forerunners: Exceptionally fast acoustic phases." *Geophysical research letters*, **34**(10).

Fee, D., Waxler, R., Assink, J., Gitterman, Y., Given, J., Coyne, J., ... & Hofstetter, R. (2013). "Overview of the 2009 and 2011 Sayarim infrasound calibration experiments." *Journal of Geophysical Research: Atmospheres*, **118**(12), 6122-6143.

Green, D. N., Waxler, R., Lalande, J. M., Velea, D., & Talmadge, C. (2018). "Regional infrasound generated by the Humming Roadrunner ground truth experiment." *Geophysical Journal International*, **214**(3), 1847-1864.

de Groot–Hedlin, C. (2008). "Finite-difference time-domain synthesis of infrasound propagation through an absorbing atmosphere." *The Journal of the Acoustical Society of America*, **124**(3), 1430-1441.

Kinney, G. F., & Graham, K. J. (1985). *Explosive shocks in air*. Berlin and New York, Springer-Verlag, 1985, 282 p.

Kulichkov, S. N. (2002). Conservation of "Acoustic momentum" during long-range infrasonic propagation in the atmosphere. *Izvestiya. Atmospheric and Oceanic Physics*, **38**(5), 582-587.

Kulichkov, S. N., Avilov, K. V., Bush, G. A., Popov, O. E., Raspopov, O. M., Baryshnikov, A. K., ... & Whitaker, R. W. (2004). "On anomalously fast infrasonic arrivals at long distances from surface explosions." *Izvestiya Atmospheric and Oceanic Physics*, **40**(1), 1-9.

576 Kulichkov, S. N., Chunchuzov, I. P., & Popov, O. I. (2010). "Simulating the influence of an
577 atmospheric fine inhomogeneous structure on long-range propagation of pulsed acoustic
578 signals." *Izvestiya, Atmospheric and Oceanic Physics*, **46**(1), 60-68.

579 Lalande, J. M., & Waxler, R. (2016). "The interaction between infrasonic waves and gravity wave
580 perturbations: Application to observations using UTTR rocket motor fuel elimination events."
581 *Journal of Geophysical Research: Atmospheres*, **121**(10), 5585-5600.

582 Lingevitch, J. F., Collins, M. D., & Siegmann, W. L. (1999). "Parabolic equations for gravity and
583 acousto-gravity waves." *J. Acoust. Soc. Am.*, **105**(6), pp. 3049-3056.

584 Lonzaga, J. B., Waxler, R. M., Assink, J. D., & Talmadge, C. L. (2015). "Modelling waveforms of
585 infrasound arrivals from impulsive sources using weakly non-linear ray theory." *Geophysical*
586 *Journal International*, **200**(3), 1347-1361.

587 Marcillo, O., Arrowsmith, S., Whitaker, R., Anderson, D., Nippress, A., Green, D. N., & Drob,
588 D., (2013). Using physics-based priors in a Bayesian algorithm to enhance infrasound source
589 location. *Geophysical Journal International*, **196**(1), 375-385.

590 Modrak, R. T., Arrowsmith, S. J., & Anderson, D. N., (2010). A Bayesian framework for
591 infrasound location. *Geophysical Journal International*, **181**(1), 399-405.

592 Rogers, P. H., & Gardner, J. H. (1980). "Propagation of sonic booms in the thermosphere." *The*
593 *Journal of the Acoustical Society of America*, **67**(1), 78-91.

Sabatini, R., Marsden, O., Bailly, C., & Bogey, C. (2016). "A numerical study of nonlinear infrasound propagation in a windy atmosphere." The Journal of the Acoustical Society of America, **140**(1), 641-656.

Scott, J. F., Blanc-Benon, P., & Gainville, O. (2017). "Weakly nonlinear propagation of small-wavelength, impulsive acoustic waves in a general atmosphere." *Wave Motion*, 72, 41-61.

Stoer, J., & Bulirsch, R. (2013). "Chapter 7: Ordinary Differential Equations" In *Introduction to Numerical Analysis (Vol. 12).* (pp. 465-618) Springer Science & Business Media.

Sutherland, L. C., & Bass, H. E., (2004). Atmospheric absorption in the atmosphere up to 160 km. *The Journal of the Acoustical Society of America*, **115**(3), pp.1012-1032.

Vergoz, J., Le Pichon, A., & Millet, C. (2019). "The antares explosion observed by the USArray: an unprecedented collection of infrasound phases recorded from the same event." In *Infrasound Monitoring for Atmospheric Studies* (pp. 349-386). Springer, Cham.

Waxler, R., Evers, L. G., Assink, J., & Blom, P. (2015). "The stratospheric arrival pair in infrasound propagation." *J. Acoust. Soc. Am.*, **137**(4), 1846-1856.

Waxler, R. (2016, August). "An overview of infrasound propagation." In *INTER-NOISE and NOISE-CON Congress and Conference Proceedings* (Vol. 253, No. 1, pp. 7229-7237). Institute of Noise Control Engineering.

611 Waxler, R., Assink, J., & Velea, D. (2017). "Modal expansions for infrasound propagation and
612 their implications for ground-to-ground propagation." *J. Acoust. Soc. Am.*, **141**(2), 1290-1307.

613 Waxler, R., & Assink, J. (2019). "Propagation modeling through realistic atmosphere and
614 benchmarking." In *Infrasound monitoring for atmospheric studies* (pp. 509-549). Springer,
615 Cham.

616 United States National Oceanic, Atmospheric Administration (NOAA) & United States Air
617 Force. (1976). US standard atmosphere, 1976 (Vol. 76, No. 1562). National Oceanic and
618 Atmospheric Administration.